Passive control of viscous flow via elastic snap-through

Michael Gomez,[1] Derek E. Moulton,[1] and Dominic Vella[1,*]

[1] *Mathematical Institute, Andrew Wiles Building, University of Oxford, Woodstock Road, Oxford OX2 6GG, UK*

We demonstrate the passive control of viscous flow in a channel by using an elastic arch embedded in the flow. Depending on the fluid flux, the arch may 'snap' between two states — constricting and unconstricting — that differ in hydraulic conductivity by up to an order of magnitude. We use a combination of experiments at a macroscopic scale and theory to study the constricting and unconstricting states, and determine the critical flux required to transition between them. We show that such a device may be precisely tuned for use in a range of applications, and in particular has potential as a passive microfluidic fuse to prevent excessive fluxes in rigid-walled channels.

Elastic elements are finding increasing utility in engineering design, from aeronautics to architecture [1]. The potential for passive control offered by morphable components holds particular promise in microfluidics where a library of design considerations to control the flow of fluid exists, including the geometrical, chemical and mechanical characteristics of the channel [2]. Of these, many are fixed at the design stage (e.g. the network connectivity) and are difficult to change subsequently, while others can be changed actively during operation. For example, the Quake valve [3, 4] allows flow in a primary channel to be blocked off by inflating control channels. Channel flexibility has been exploited to control flows by bending the device [5], applying a varying potential difference to create a microfluidic pump [6] or simply by turning mechanical screws to constrict flow [7].

The above examples have two features in common: they are actively controlled and generate a smoothly transitioning fluid flow. However, this active control may mean that miniaturization becomes difficult if, for example, additional power sources are required. Passive control, the ability of a flow to self-regulate, is then desirable, and has led to the development of passive pumps in microfluidic devices [8, 9]. In other circumstances, a rapid and switch-like response may also be useful, for example as a logic element in microfluidic circuits [10], in fluidic gating [11], or as a fuse to limit the fluid flux within a channel to some predetermined maximum.

Elastic 'snap-through', in which a system rapidly transitions from one state to another (just as an umbrella rapidly inverts in high winds) is a natural candidate for such a passive control mechanism: snap-through is generally fast, repeatable, and provides a large shape change. Snap-through has been harnessed in biology and engineering to generate fast motions between two states [12–16]. Previous studies have focussed on snapping due to dry, mechanical loads including indentation [17], end rotation [18] and electrostatic forces [19], or capillary forces in wet systems [20]. However, snap-through caused by bulk fluid flow remains relatively unexplored. Similarly, the use of elastic deformation to control fluid flows has largely focussed on the development of fluidic diodes and valves [4, 8].

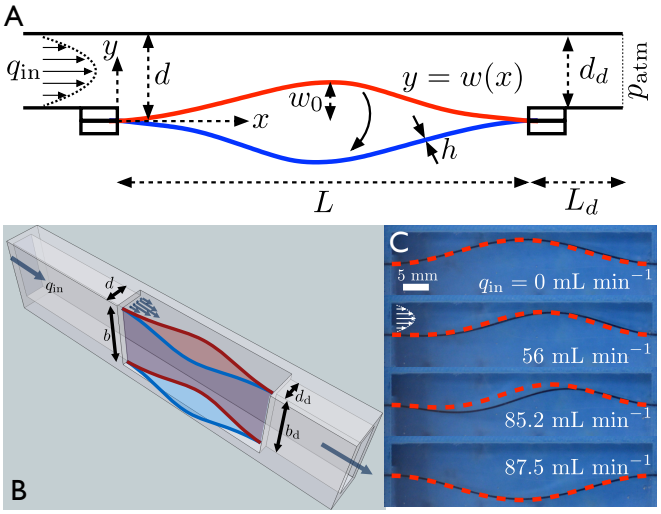

FIG. 1: Viscous flow through a channel containing a flexible wall. (A) A thin elastic strip, buckled into an arch, initially constricts part of a channel (red shape). At higher flow rates, the arch rapidly snaps through (blue shape); the flow is then unconstricted and the channel's conductivity increases. (B) Three-dimensional view showing the finite channel depth. (C) Shapes of the arch during a snapping experiment ($h = 0.25$ mm, $w_0 = 4.7$ mm, $\eta = 1.60 \pm 0.10$ Pa s), together with the shapes predicted by our beam-lubrication model (red dashed curves).

To illustrate the mechanics of snap-through and its possible use to control flow, we performed macroscopic experiments. Flow occurs in a channel of rectangular cross-section (width $d = 6$ mm, depth $b = 23$ mm) in which one of the bounding walls is replaced by a flexible strip of bi-axially oriented polyethylene terephthalate (PET) film (Young's modulus $E = 5.72 \pm 0.52$ GPa). The rigid portion of the channel was 3D printed, with one of the walls fabricated from transparent acrylic to visualize the flow-induced deformation of the flexible element. The ends of the strip are clamped parallel to the flow direction, a distance $L = 50$ mm apart, using thin notches built into the surrounding channel walls (see fig. 1a). The bending stiffness of the strip was varied by using different

thicknesses $h \in \{0.1, 0.25\}$ mm [31].

A controlled volumetric flux, $q_{\rm in}$, of glycerol (viscosity range 1.10 Pa s $\leq \eta \leq$ 1.80 Pa s) was introduced using a syringe pump (Harvard Apparatus PHD Ultra Standard Infuse/Withdraw 70-3006). Next to the arch the (reduced) Reynolds number is Re $= O(10^{-2})$ so that fluid inertia is negligible. We measured the fluid pressure at the upstream end of the arch using a voltage-output pressure transducer (OMEGA PX40-50BHG5V). We were able to accurately measure pressures larger than 140 Pa with typical uncertainty ±20 Pa (due to uncertainties in the voltage measurement).

A key geometric parameter is the relative height of the arch in the absence of flow, w_0, to the upstream channel width d (fig. 1a). This arch height was varied within the channel assembly by changing the length of the strip prior to clamping. The difference between the natural length of the strip, $L_{\rm strip}$, and the horizontal distance between the two clamping points is referred to as the end–shortening $\Delta L = L_{\rm strip} - L \ll L$; for shallow arches ΔL is related to the arch amplitude by $w_0 \approx 2(L\,\Delta L)^{1/2}/\pi$ (using the Euler-buckling mode $w(x) = w_0\big[1 - \cos(2\pi x/L)\big]/2$ [5]).

At the start of each experiment, the arch was placed in a constricting state with its midpoint directed into the channel (fig. 1a). To determine the dependence of the system on the fluid flux, $q_{\rm in}$, this flux was ramped from zero at a rate $\dot{q}_{\rm in} = 2$ mL min^{-2} (when $h = 0.1$ mm) or $\dot{q}_{\rm in} = 70$ mL min^{-2} (when $h = 0.25$ mm). In both cases the ratio of the convective timescale ($Lbd/q_{\rm in}$) to the ramping timescale ($q_{\rm in}/\dot{q}_{\rm in}$) is $O(0.1)$ at the point of snap-through — ramping occurs approximately quasi-statically. A digital camera mounted above the acrylic wall recorded the shape of the arch and allowed the midpoint height w_0 to be measured to an accuracy ±0.2 mm.

Snapshots of the arch shape as $q_{\rm in}$ changes are shown in fig. 1c (for movies see [31]). As $q_{\rm in}$ increases, the shape of the arch changes only slightly at first, developing a small asymmetry due to the pressure gradient that drives the flow. However, at a critical value of $q_{\rm in}$ the shape changes dramatically: the arch suddenly adopts the opposite curvature (last panel in fig. 1c) and, if the flux $q_{\rm in}$ is subsequently reduced, the arch remains in this 'snapped', unconstricting configuration.

To quantify the behavior of this flexible channel, we measure the pressure at the upstream end of the arch, $p(0)$, as a function of the imposed flux; results for different initial arch heights are shown in fig. 2a. For small arch heights, the pressure increases approximately linearly with $q_{\rm in}$ before snap-through, as would be expected for Poiseuille flow in a rigid channel. However, for larger arch heights, $w_0/d \nearrow 1$, the contrast with Poiseuille flow becomes apparent: the pressure changes nonlinearly with $q_{\rm in}$ and is even non-monotonic, reaching a maximum prior to snapping (fig. 2a). Over a large range of fluxes, the channel therefore has a softening property whereby the effective hydraulic conductivity, which we define as $k = q_{\rm in}/p(0)$, increases smoothly with increasing flux (fig. 2c).

Snap-through causes even more significant changes: the pressure drops discontinuously, even though the flux has increased, because the channel switches from a constricted state to an unconstricted state. The contrast between the channel conductivities in the two states is large and grows as the arch height, w_0, grows (fig. 2c). The system exhibits hysteresis since the snapped configuration remains stable if $q_{\rm in}$ is decreased (fig. 2b).

A key quantity of interest is the critical flux, $q_{\rm snap}$, at which snap-through occurs; fig. 3 (inset) shows that this depends not only on the arch height, w_0, but also on the flexibility of the arch and the liquid's properties. Surprisingly, we find that the value of $q_{\rm snap}$ is a non-monotonic function of arch height: for given material parameters, a maximum value of $q_{\rm snap}$ is obtained at $w_0/d \approx 0.5$.

To gain theoretical insight we first note that the deflection δ of an elastic strip, of length L and bending stiffness B, due to a force F (per unit length) scales as $\delta \sim FL^3/B$ [21]. Here the typical force $F \sim pL$, where p is the fluid pressure, and hence the induced deformation $\delta_{\rm flow} \sim pL^4/B$. The Poiseuille law [22] for the pressure drop along a slender channel of width d and depth b, with an obstruction of maximum size $w_{\rm max}$, suggests that $p \sim \eta L q_{\rm in}/[b(d - w_{\rm max})^3]$. This pressure estimate then gives $\delta_{\rm flow} \sim \eta L^5 q_{\rm in}/[Bb(d - w_{\rm max})^3]$, which may be compared with the initial arch height w_0 to estimate the threshold flux for snap-through (analogously to point indentation [17]) as

$$q_{\rm snap} \sim \frac{Bb\,(d - w_{\rm max})^3}{\eta L^5} w_0. \qquad (1)$$

This may be written in terms of the channel blocking parameter, $W_0 = w_0/d$, as

$$Q_{\rm snap} \sim W_0 \left(1 - \frac{w_{\rm max}}{d}\right)^3, \qquad (2)$$

where a dimensionless fluid flux is

$$Q = \frac{\eta L^5}{Bbd^4} q_{\rm in}. \qquad (3)$$

This non-dimensionalization provides an excellent collapse of the experimental data onto a single master curve (fig. 3). Moreover, the non-monotonic behavior observed in fig. 3 is qualitatively explained by (2): for small channel blocking parameter, $W_0 = w_0/d \ll 1$, the maximum arch displacement $w_{\rm max} \ll d$, and hence $Q_{\rm snap} \sim W_0$. However, when $w_{\rm max}$ becomes comparable to the channel width d ($W_0 \nearrow 1$), $Q_{\rm snap}$ decreases.

To go beyond these scaling arguments, we formulate a model coupling the shape of the arch with the fluid pressure by exploiting the thin-film geometry and the shallow slope of the arch. This allows us to use the one-dimensional linear beam equation [23]

$$B\frac{\mathrm{d}^4 w}{\mathrm{d}x^4} + T\frac{\mathrm{d}^2 w}{\mathrm{d}x^2} + p(x) = 0, \qquad 0 < x < L, \qquad (4)$$

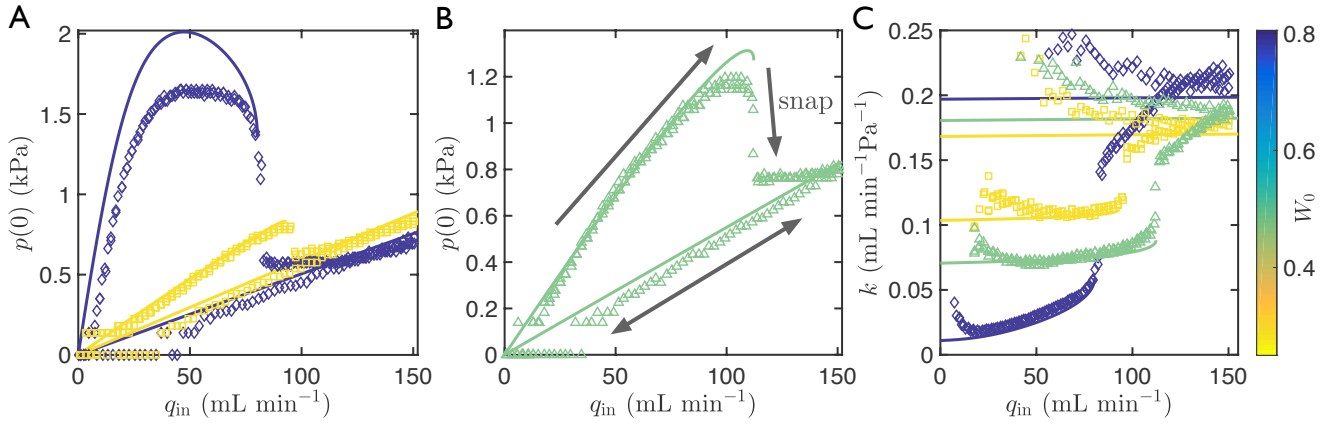

FIG. 2: Pressure-flux relations for a flexible channel ($h = 0.25$ mm, $\eta = 1.60\pm0.10$ Pa s). (A) Evolution of the upstream pressure, $p(0)$, for different channel blocking parameters $W_0 = w_0/d$ (indicated by the colorbar). For each W_0, three data sets through the snapping transition are shown, together with a fourth in which the beam remains in the snapped configuration throughout (symbols). Predictions from the beam-lubrication model, (6), are also shown (solid curves). (The snapping transition appears continuous in experiments because the arch motion is overdamped.) (B) The hysteresis loop highlighted for intermediate W_0. (C) The effective hydraulic conductivity $k = q_{\rm in}/p(0)$ is plotted for the same data (with $p(0) > 140$ Pa, to avoid noise due to inaccurate readings at low pressure.)

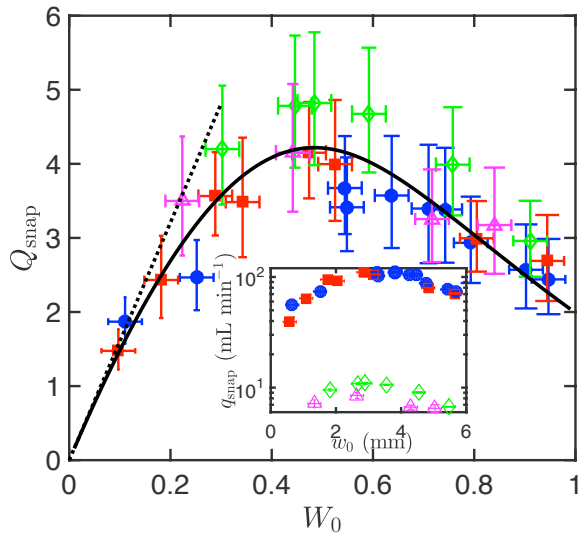

FIG. 3: Critical flux for snap-through. Inset: Experimentally measured snap-through flux, $q_{\rm snap}$ (averaged over three runs), as a function of the initial midpoint height, w_0. Data is shown for $h = 0.25$ mm with $\eta = 1.38 \pm 0.17$ Pa s (blue circles) and $\eta = 1.61 \pm 0.18$ Pa s (red squares); and for $h = 0.1$ mm with $\eta = 1.20\pm0.10$ Pa s (green diamonds) and $\eta = 1.33\pm0.08$ Pa s (magenta triangles; increasing $q_{\rm in}$ in steps of 0.25 mL min^{-1} every minute rather than ramping). Horizontal error bars correspond to the ±0.2 mm uncertainty in w_0; vertical error bars give the standard deviation of the measured values. Main plot: Rescaling to plot the dimensionless flux $Q_{\rm snap} = \eta L^5 q_{\rm snap}/(Bbd^4)$ in terms of the channel blocking parameter $W_0 = w_0/d$, the data collapse onto the prediction of our numerical analysis (solid black curve). Vertical error bars here also account for uncertainties in the bending stiffness B and viscosity η. Also plotted is the asymptotic result $Q_{\rm snap} \approx 16 W_0$ valid for $W_0 \ll 1$ [31] (black dotted line).

to describe the transverse displacement, $w(x)$, of the arch, with T the compressive force in the arch, and $p(x)$ the hydrodynamic pressure. (An analysis of the shear stress exerted on the arch by the fluid shows [24] that the compressive force T is spatially uniform provided that $|{\rm d}w/{\rm d}x| \ll 1$, as already assumed in using the linear beam equation.) Assuming that the strip is inextensible [17], the imposed end-shortening ΔL leads to the constraint

$$\int_0^L \left(\frac{{\rm d}w}{{\rm d}x}\right)^2 {\rm d}x = 2\Delta L. \qquad (5)$$

The ends of the arch, at $x = 0$ and $x = L$, are clamped i.e. $w(0) = w'(0) = w(L) = w'(L) = 0$ (with primes denoting differentiation with respect to x).

To determine the pressure within the liquid, $p(x)$, we use lubrication theory [25], consistent with our assumption of small slopes, $|{\rm d}w/{\rm d}x| \ll 1$. Using standard methods, the pressure may be expressed [31] as

$$p(x) = p(L) + \frac{12\eta q_{\rm in}}{b} \int_x^L \frac{K(w(\xi))}{[d - w(\xi)]^3}\, {\rm d}\xi, \qquad (6)$$

where we use a geometric correction factor [2, 22]

$$K(w) = \left[1 - 6\left(\frac{2}{\pi}\right)^5 \frac{d-w}{b}\right]^{-1},$$

to account for the finite depth of the channel. The pressure at the downstream end of the arch depends on the downstream geometry of the channel (denoted with subscript d, as in fig. 1a) and is given by

$$p(L) = \frac{12\eta q_{\rm in} L_{\rm d}}{b_{\rm d} d_{\rm d}^3}\left[1 - 6\left(\frac{2}{\pi}\right)^5 \frac{d_{\rm d}}{b_{\rm d}}\right]^{-1},$$

measured relative to the ambient pressure (which is imposed at the end of the channel, $x = L + L_d$).

We introduce the dimensionless variables $X = x/L$, $W = w/d$, and $P = p/p_*$ where $p_* = Bd/L^4$ is the pressure scale introduced by the beam equation (4). With this non-dimensionalization, there are two key governing parameters: the dimensionless flux Q, defined in (3), and the channel blocking parameter $W_0 = w_0/d \approx 2(L\,\Delta L)^{1/2}/(\pi d)$.

The dimensionless versions of equations (4)–(6) may be solved for given values of W_0 and Q to determine both the arch shape and the dimensionless pressure field, $P(X)$. Predicted arch shapes are shown in fig. 1c, superimposed on the experimentally observed shapes; the agreement between theory and experiment is very good for all values of Q investigated, including beyond the snap-through transition. The discrepancy is largest close to snap-through (third panel of fig. 1c), since the sensitivity to the precise value of Q is largest here. The predicted (dimensional) upstream pressure $p(0)$ is shown in fig. 2a,b, with corresponding conductivities $k = q_{in}/p(0)$ plotted in fig. 2c; both generally agree well with experiment (errors in the conductivity at low fluxes are due to uncertainties in the measurement of low pressures). Close to total blocking, $W_0 \approx 1$, there is a systematic error in the model, which we attribute to the relatively large arch slopes at the midpoint that are not captured by our use of lubrication and linear beam theories. Nevertheless, the model captures the qualitative behavior of the pressure throughout, including the non-monotonicity of $p(0)$ as a function of q_{in}.

A numerical analysis of the problem shows [31] that the snap-through transition is a saddle-node bifurcation: the constricting state ceases to exist at a critical value $Q = Q_{snap}$ without first becoming unstable [17]. The numerically determined value of $Q_{snap}(W_0)$ reproduces the experimentally determined master curve; see fig. 3. For $W_0 \ll 1$, an asymptotic analysis shows that $Q_{snap} \approx 16W_0$, reproducing the linear scaling of (2). For $0.1 \lesssim W_0 \leq 1$, we find that Q_{snap} varies by less than a factor of 2, with $2 \lesssim Q_{snap} \lesssim 4$.

The system we have presented is irreversible — post snapping the strip cannot return to the constricting state without direct intervention. However, this is not a fundamental feature: reversibility may be accomplished by introducing flow in an access channel to the region below the arch, to snap the arch back to its original position (see e.g. [11]). Alternatively, an automatic reset, which may be desirable in some applications, may be easily achieved by clamping one end of the arch at an angle to the horizontal [18, 26] so that the snapped configuration is not in equilibrium in the absence of flow. In this case, the system exhibits a hysteresis loop with an increase in the input flux generating a snap in one direction, and a subsequent (further) decrease in flux causing a snap back (see fig. S6 of [31]).

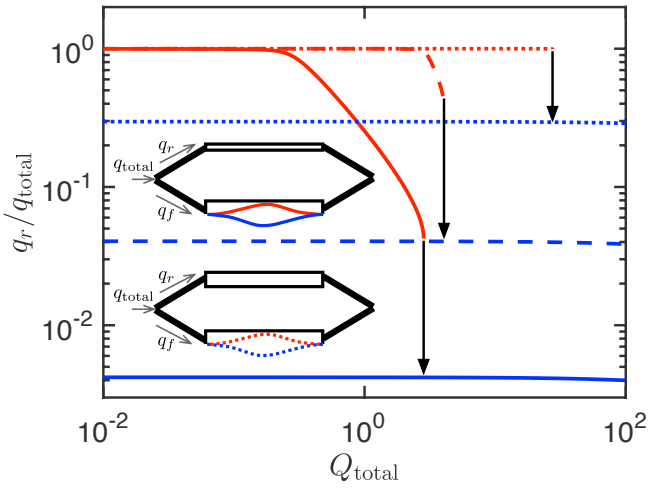

FIG. 4: Flow limiting using snap-through. Inset: A channel with a flexible wall is connected in parallel to a rigid channel of constant conductivity (schematics not drawn to scale). Main figure: For low total fluxes $Q_{total} = \eta L^5 q_{total}/(Bbd^4)$ with the flexible channel constricting (red curves), almost all of the flow is directed through the rigid channel, i.e. $q_r/q_{total} \approx 1$. This is diverted through the flexible channel as soon as the arch snaps (blue curves). Here $W_0 = 0.99$ and numerical results are shown for different conductivity ratios λ between the channels: $\lambda = 10^{-2}$ (solid curves), $\lambda = 10^{-1}$ (dashed curves) and $\lambda = 1$ (dotted curves).

In both the irreversible and reversible scenarios, the quantitative features of the mechanism (e.g. the critical snapping fluxes and the corresponding change in conductivity) may be precisely tuned. Therefore, with an arch element coupled to other components, a range of design possibilities opens up. For example, in fig. 4 we demonstrate the potential for a passive fluid 'fuse'. Here we have placed an arch element in parallel with another, entirely rigid, channel (fig. 4a inset). Denoting the (constant) effective hydraulic conductivity of the rigid channel by k_r, and the (variable) conductivity of the flexible channel by $k_f(q_f)$, the ratio of the fluxes through each of the two channels is $q_r/q_f = k_r/k_f$ by the Poiseuille law.

Denoting the total flux $q_{total} = q_f + q_r$ and calculating q_r/q_{total}, the fraction of the total flux that passes through the rigid channel, we find a switch-like response (fig. 4): while the arch is in a constricting shape, most of the fluid passes through the rigid channel, but once the arch snaps, much of the fluid is diverted to the now unconstricted flexible channel. The rigid channel is effectively 'short-circuited'. The efficiency of the fuse, defined as the decrease in q_r caused by snap-through divided by its value prior to snap-through, may be tuned by varying the geometric parameters of each channel [31].

We have shown at a laboratory scale that the pressure gradient associated with a viscous flow can be used to cause snap-through of an embedded elastic element. The system considered has a number of novel flow prop-

erties including a highly nonlinear pressure-flux relationship, discontinuous conductivity and history dependence. These properties may find application in microfluidic systems such as cell-sorting or, as we have shown, provide a means to protect microfluidic systems from high fluxes. Similarly, the discontinuous transition we observe is similar to that seen in capillary burst valves [27] and gas release valves [28]. A simple analysis [31] shows that when scaling down to the microscale, the expected range of snap-through fluxes are well within experimentally obtainable values. For such applications our study thus provides a first analysis of flow-induced snapping and guidance for choosing material parameters to tune the critical flux. While viscous flow control is readily applicable to microfluidics, the passive control and rapid transition capabilities of elastic materials is increasingly being exploited more broadly, e.g. in soft robotics and morphing skins [29, 30]. Developing theoretical models that provide intuition and facilitate device optimization will be critical in these burgeoning fields of technology.

The research leading to these results has received funding from the European Research Council under the European Union's Horizon 2020 Programme / ERC Grant Agreement no. 637334 (DV). We are grateful to Clément le Gouellec for early experiments in a related system, Alain Goriely for 3D printing, Chris MacMinn for laser cutting, as well as the John Fell Oxford University Press (OUP) Research Fund (award number 132/012).

* Electronic address: dominic.vella@maths.ox.ac.uk

[1] C. K. Khoo, F. Salim, and J. Burry, Int. J. Arch. Comput. **9**, 397 (2011).
[2] H. A. Stone, A. D. Stroock, and A. Ajdari, Annu. Rev. Fluid Mech. **36**, 381 (2004).
[3] M. A. Unger, H. P. Chou, T. Thorsen, A. Scherer, and S. R. Quake, Science **288**, 113 (2000).
[4] K. W. Oh and C. H. Ahn, J. Micromech. Microengng **16**, R13 (2006).
[5] D. P. Holmes, B. Tavakol, G. Froehlicher, and H. A. Stone, Soft Matter **9**, 7049 (2013).
[6] B. Tavakol, M. Bozlar, C. Punckt, G. Froehlicher, H. A. Stone, I. A. Aksay, and D. P. Holmes, Soft Matter **10**, 4789 (2014).
[7] D. B. Weibel, M. Kruithof, S. Potenta, S. K. Sia, A. Lee, and G. M. Whitesides, Anal. Chem. **77**, 4726 (2005).
[8] D. C. Leslie, C. J. Easley, E. Seker, J. M. Karlinsey, M. Utz, M. R. Begley, and J. P. Landers, Nat. Phys. **5**, 231 (2009).
[9] A. E. Hosoi and L. Mahadevan, Phys. Rev. Lett. **93**, 137802 (2004).
[10] J. A. Weaver, J. Melin, D. Stark, S. R. Quake, and M. A. Horowitz, Nat. Phys. **6**, 218 (2010).
[11] B. Mosadegh, C.-H. Kuo, Y.-C. Tung, Y.-s. Torisawa, T. Bersano-Begey, H. Tavana, and S. Takayama, Nat. Phys. **6**, 433 (2010).
[12] Y. Forterre, J. M. Skotheim, J. Dumais, and L. Mahadevan, Nature **433**, 421 (2005).
[13] J. S. Han, J. S. Ko, and J. G. Korvink, J. Micromech. Microengng **14**, 1585 (2004).
[14] A. Brinkmeyer, M. Santer, A. Pirrera, and P. Weaver, Int. J. Solids Struct. **49**, 1077 (2012).
[15] D. P. Holmes and A. J. Crosby, Adv. Mater. **19**, 3589 (2007).
[16] J. T. B. Overvelde, T. Kloeka, J. J. A. D'haen, and K. Bertoldi, Proc. Natl Acad. Sci. USA **112**, 10863 (2015).
[17] A. Pandey, D. E. Moulton, D. Vella, and D. P. Holmes, EPL **105**, 24001 (2014).
[18] M. Gomez, D. E. Moulton, and D. Vella, Nat. Phys. **13**, 142 (2017).
[19] S. Krylov, B. R. Ilic, D. Schreiber, S. Seretensky, and H. Craighead, J. Micromech. Microengng **18**, 055026 (2008).
[20] A. Fargette, S. Neukirch, and A. Antkowiak, Phys. Rev. Lett. **112**, 137802 (2014).
[21] S. P. Timoshenko and J. N. Goodier, *Theory of Elasticity*, McGraw Hill, 1970.
[22] J. Happel and H. Brenner, *Low Reynolds number hydrodynamics*, Kluwer, 1983.
[23] P. Howell, G. Kozyreff, and J. Ockendon, *Applied Solid Mechanics*, Cambridge University Press, 2009.
[24] O. Kodio, I. M. Griffiths, and D. Vella, Phys. Rev. Fluids **2**, 014202 (2017).
[25] L. G. Leal, *Advanced Transport Phenomena: Fluid Mechanics and Convective Transport Processes*, Cambridge University Press, 2007.
[26] G. Arena, R. M. J. Groh, A. Brinkmeyer, R. Theunissen, P. M. Weaver, and A. Pirrera, Proc. R. Soc. A **473**, 20170334 (2017).
[27] H. Cho, H.-Y. Kim, J. Y. Kang, and T. S. Kim, J. Colloid Interf. Sci. **306**, 379 (2007).
[28] D. Kim, Y. W. Hwang, and S.-J. Park, Microsyst. Technol. **15**, 919 (2009).
[29] J. T. B. Overvelde, T. Kloek, J. J. A. D'haen, and K. Bertoldi, Proc. Natl Acad. Sci. **112**, 10863 (2015).
[30] C. Thill, J. Etches, I. Bond, K. Potter, and P. Weaver, Aero. J. **112**, 117 (2008).
[31] See Supplemental Material at http://link.aps.org/ supplemental/ for further details of experiments and theoretical calculations.